A. STAMPANONI-
PANARIELLO[1]
D.N. KOZLOV[2]
P.P. RADI[3], ✉
B. HEMMERLING[3]

Gas-phase diagnostics by laser-induced gratings II. Experiments

[1]Institute for Quantum Electronics, ETH Zürich, 8093 Zürich, Switzerland
[2]A.M. Prokhorov General Physics Institute, 119991 Moscow, Russia
[3]Paul Scherrer Institut, 5232 Villigen PSI, Switzerland

ABSTRACT In this article we review the results achieved in the past ten years at the Paul Scherrer Institute on the topic of diagnostics in the gas phase by laser-induced gratings (LIGs). The technique has been applied for thermometry in air and in flames at different pressures, for flow velocimetry, for concentration measurements, and for imaging purposes. The influence of collisional energy-transfer and relaxation processes in molecules on the temporal evolution of the LIG signals has also been investigated. It has been demonstrated that, for molecules with a low fluorescence quantum yield, excitation of laser-induced thermal gratings can be used as a sensitive spectroscopic tool. For the quantitative interpretation of the experiments shown in this work, the findings presented in the companion paper [1] have been used.

1 Introduction

With the progress of technology, laser sources have become extremely versatile and affordable. They have found a variety of application fields in medicine, industry, and science and – in particular – in the field of combustion diagnostics. With the concern of hydrocarbon fuel source availability and environmental considerations, combustion processes need to become more efficient and more clean. To test and validate combustor design and to verify predictive computational results, it is necessary to measure the temperature and chemical composition of the combustion products. However, there are some limitations in probing combustion processes to the extent that is required for both empirical and theoretical advances. These limitations arise for two primary reasons. First of all, the high temperatures and heat-transfer rates render these systems difficult to probe physically with the desired space and time resolutions. In addition, high demands on the probe materials are imposed to endure the harsh environment. Furthermore, combustion processes are delicately sta-

bilized and thus easily altered by physical intrusion. Optical techniques have been recognized by combustion researchers for their potential to overcome these limitations. Laser-based techniques allow the remote, non-intrusive, in situ, spatially and temporally resolved measurement of important chemical parameters [2]. However, laser techniques are not without disadvantages: a major limitation is the requirement of an optical access to the test volume. In addition, at present they require a fairly high level of operator skill. All of the instruments required, e.g. lasers, detectors, spectrographs, etc. are commercially available. Nevertheless, there has been little commercial integration of the discrete items into complete 'turnkey' instruments, at least in regard to techniques for species and temperature measurements. Furthermore, for the correct determination of temperature and concentration by laser spectroscopic techniques, a deep understanding of all physical processes involved is essential. Consequently, an elaborate analysis of the signal has to be performed for the quantitative determination of the parameters of interest. The measured spectra need to be carefully modeled and this usually requires computationally intensive numerical programming. For these reasons the optical diagnostic techniques continue to be developed and improved in order to render them more versatile and user friendly. Laser-induced gratings (LIGs) are a relatively new and promising optical technique for the diagnostics in the gas phase. By the temporally resolved detection of a continuous-wave (cw) probe beam diffracted by LIGs, various thermodynamic properties of the medium can be inferred such as the temperature, the viscosity, the thermal conductivity, and, under favorable conditions, the species concentration. If a laser-induced grating is generated in a flow, the scattered probe beam will exhibit frequency components that are shifted due to the Doppler effect by an amount which is proportional to the flow velocity. From the analysis of the temporal evolution of the diffracted beam intensity, the flow velocity can thus be determined without seeding the flow.

Methods based on LIGs are closely related to other nonlinear techniques that have been developed recently for diagnostics in combustion environments. For example, the interest for thermal LIGs arises on one hand because of the need to account for their contribution in four-wave-mixing (FWM) experiments. In fact, at higher pressure the thermal LIGs'

✉ Fax: +41-1-633-13-54, E-mail: radi@phys.ethz.ch

contribution to FWM signals becomes important and has to be quantified for a correct interpretation of the results. On the other hand, thermal LIGs themselves have a potential for diagnostic applications in the gas phase and for fundamental research. For example, they have been employed to investigate quenching processes [3–7] and for the measurement of species concentrations with low fluorescence quantum yields [3]. Schlamp et al. [8] have studied the accuracy and uncertainty of single-shot non-resonant laser-induced thermal acoustics measurements of the speed of sound and the thermal diffusivity in unseeded atmospheric air from electrostrictive gratings as a function of the laser power settings. The transport properties of high-pressure fluids have been measured by Kimura et al. [9]. Latzel et al. [10] have employed thermal gratings to determine acoustic velocity and thermal conductivity of gaseous mixtures of ethylene and nitrogen–helium. Furthermore, thermal LIGs have been proposed as an alternative method to coherent anti-Stokes Raman scattering (CARS) thermometry, which is a very reliable and versatile tool for measurements of temperatures. CARS, however, requires both a complex experimental setup and an elaborate procedure for the data analysis [11]. Using laser-induced thermal gratings, the temperature can be determined by a simple frequency analysis of the oscillations of the LIGs' diffraction efficiency if the composition of the measured medium is known. Williams et al. [12] have applied thermal gratings for the measurement of temperature in an atmospheric pressure H_2/O_2 flame. Barker et al. [13] have employed thermal gratings for single-shot temperature measurements in supersonic air flows. Schlamp et al. [14] have used laser-induced thermal acoustics (LITA) with heterodyne detection to measure simultaneously and in a single laser pulse the sound speed and flow velocity of NO_2-seeded air in a low-speed wind tunnel up to Mach number $M = 0.1$. Schlamp and Sobota [15] have proposed the possibility of applying LITA to measure concentration of a resonantly excited seed species diluted within a non-resonantly excited species by comparing the contributions from thermalization and electrostriction in the combined signal.

Since soot particles which are present in flames absorb widely across the electromagnetic spectrum, it is possible to generate thermal gratings with almost any pulsed laser source. Based on this idea, Brown and Roberts [16] recognized the potential of LIGs to perform temperature measurements in sooty flames.

The availability of fixed-frequency laser sources has favored the use of electrostrictive LIGs for several applications, e.g. for the study of acoustic modes and their attenuation and coupling in condensed matter [17–19]. For diagnostic purposes in the gas phase, electrostrictive LIGs have been applied to image a stream of helium in air [20], to determine acoustic velocity and acoustic attenuation in gases [21, 22], to measure temperatures in air and flames [23], to determine the concentration of binary gas mixtures [24–26], and to measure simultaneously flow velocities and temperatures [27, 28].

This article comprises the results of experimental investigations achieved in the past ten years at the Paul Scherrer Institute in Villigen (CH) in collaboration with the A.M. Prokhorov General Physics Institute of Moscow; see Refs. [3, 4, 7, 20, 23–30]. Together with its companion article [1] it is intended to be a useful tool to anyone who plans to apply the LIG technique for diagnostics in the gas phase.

In the following the specific diagnostic applications of the technique presented in this work are outlined.

In Sect. 2.1 we describe the application method for thermometry in ambient air up to 1400 K and in premixed CH_4/air flames at atmospheric and higher pressures (up to 25 bar). The methodology of concentration measurements by laser-induced gratings is presented in Sect. 2.2. Laser-induced electrostrictive gratings have been applied for the determination of acoustic velocities in gases and for the measurement of the composition of binary isothermal gas mixtures of N_2/CH_4 and N_2/H_2. By employing thermal gratings, we have been able to detect the isotopic molecule $^{16}O^{18}O$ in its natural abundance, thus demonstrating the high sensitivity of this method. Investigations of energy-transfer processes are described in Sect. 2.3. We have selected oxygen as an example of a molecule that can be excited via a magnetic dipole-allowed transition with a small transition probability. Rotational redistribution and electronic quenching determine the temporal evolution of the scattering diffraction efficiency. If quenching is efficient, laser-induced thermal gratings can be employed as a very sensitive spectroscopic tool. It is not always possible to find a dipole-allowed transition within the spectral range accessible by lasers. In this case it is convenient to excite Raman-active transitions for the generation of thermal LIGs. As an example for the generation of thermal gratings by Raman excitation, we have selected carbon dioxide [4]. In Sect. 2.4 electrostrictive LIGs have been used for the simultaneous, instantaneous, non-intrusive, and remote measurement of flow velocities and temperatures in air flows in the ranges 10–100 m/s and 295–600 K, respectively. In Sect. 2.5 a two-dimensional setup of the technique has been applied to visualize a helium stream in air and to map soot in an acetylene/air diffusion flame.

In Sect. 3, the results are recapitulated and possible future work is outlined in the field of laser diagnostics by coherent techniques.

2   Gas-phase diagnostics by transient laser-induced gratings

2.1   *Temperature measurements*

One of the most established techniques for the determination of temperatures is coherent anti-Stokes Raman scattering (CARS); see Ref. [2] and references therein. Among the numerous advantages of CARS thermometry the two most important ones are precision (± 15 K in single-shot measurements at flame temperatures [31]) and the applicability of the method in harsh environments (such as those characterized by high temperature, high pressure, and high turbulence). However, advanced experimental equipment is required: at least two lasers (a narrowband and a broadband laser), a spectrometer, and a diode array camera. Additionally, an involved data analysis is inevitable using CARS [11]. The high complexity of the method has fostered the development of alternative diagnostic approaches.

In the following, experiments for the determination of temperature in the gas phase and in flames by the LIG technique are reviewed (see Ref. [23] for details).

According to the theory presented in Ref. [1], the oscillation period of the diffraction efficiency of a LIG is given by

$$T_g = \frac{\Lambda}{f v_S}, \tag{1}$$

where $f = 1$ for a thermal LIG and $f = 2$ for an electrostrictive LIG. If the fringe spacing Λ of the LIG is known, the adiabatic sound velocity in the medium is deduced from the oscillation period of the LIG diffraction efficiency. For an ideal gas the sound velocity is given by

$$v_S = \sqrt{\frac{\gamma}{M} RT}, \tag{2}$$

where T denotes the temperature, R the molar gas constant, M the molar mass, and γ the specific heat ratio. For gas mixtures M and γ are given by

$$M = \sum_{i=1}^{s} x_i M_i, \tag{3}$$

$$\gamma = \frac{\sum_{i=1}^{s} x_i M_i c_{p_i}}{\sum_{i=1}^{s} x_i M_i c_{v_i}}, \tag{4}$$

where x_i denotes the mole fraction, c_{p_i} and c_{v_i} the specific heat at constant pressure and volume of the component i, respectively, and s the number of different components. By measuring the sound velocity, the temperature is accessible for a known gas composition or, under favorable conditions, the concentration of the components in a binary mixture can be deduced if the temperature is known.

The experimental configuration used for the temperature measurements is described in detail in Ref. [23] and is depicted in Fig. 1. The procedure for the determination of the spatial resolution of the beam geometry is also described in detail in Ref. [23]. It has been found that 95% of the signal is generated in a volume extending roughly 16 mm in the direction of the bisector of the two excitation beams. This value can be

FIGURE 1 Experimental setup for temperature measurement by LIGs; CT, cylinder telescope ($f_1 = 300$ mm, $f_2 = -100$ mm); BS, beam splitter ($R = 50\%$); L1, L2, lenses ($f = 750$ mm). *Inset*: three-dimensional backward phase matching geometry; EB1, EB2 excitation beams ($\lambda = 1064$ nm, pulsed); RB, readout (or probe) beam ($\lambda = 514.5$ nm, cw)
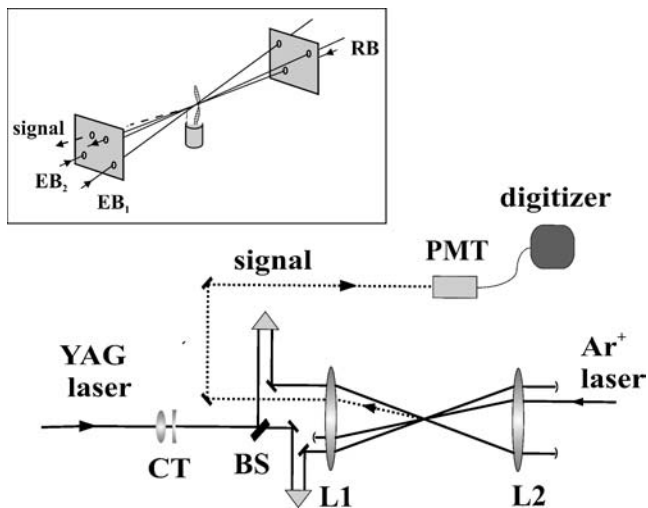
considered as an upper limit of the longitudinal size of the probe volume.

To evaluate the error of the temperatures measured by using electrostrictive LIGs, experiments in the center of an open tube furnace operated up to a maximum temperature of 1370 K have been performed. The length of the isothermal zone ($\sigma = 5$ K) exceeds 10 cm at all temperatures. The temperature reading of the furnace has been measured by a thermocouple located in the center of the heated zone. Measurements by electrostrictive LIGs have been carried out in air at different furnace temperatures. The largest error in the determination of the sound velocity results from the measurements of the angle θ between the excitation beams. Alternatively, to avoid the determination of the fringe spacing Λ by a geometric measurement of the angle θ, a reference measurement at room temperature in ambient air has been carried out. By using Eqs. (1) and (2), the measured temperature is given by

$$T = T_R \left(\frac{T_{g,R}}{T_{g,T}}\right)^2 \left(\frac{\gamma_R}{\gamma_T}\right) \left(\frac{M_T}{M_R}\right). \tag{5}$$

Here, the subscripts R and T refer to reference and temperature measurement, respectively. Changes in the gas composition caused by thermodiffusion can be neglected and, therefore, the ratio of the relative molecular masses is assumed to be unity. With increasing temperature the specific heat ratio γ decreases due to excitation of internal degrees of freedom (vibrational or rotational) of the molecules. For almost all molecular gases the rotational degrees of freedom are fully excited at room temperature (as an example we give here the values of the temperature at which the rotational degree of freedom are excited for O_2 and N_2; 2.1 K and 2.9 K, respectively). The values of the temperature necessary to excite the vibrational degree of freedom of e.g. O_2 and N_2 are 2239 K and 3352 K, respectively. Thus, at temperatures up to 1400 K the excitation of vibrational degrees of freedom gives an important contribution to the heat capacity. However, due to the high frequency of the generated acoustic waves of about 10 MHz, the dispersion caused by the different relaxation times of the internal degrees of freedom has to be considered. While the rotational and translational relaxation frequencies are well above the generated acoustic wave frequency, the vibrational relaxation frequency is around 100 kHz, depending on the humidity of air; see Ref. [32] and references therein. Therefore, the vibrational contribution to the specific heat can be safely neglected and the specific heat ratio for O_2 and N_2 can be approximated by 7/5 for the investigated temperature range, i.e. $\gamma_R/\gamma_T \approx 1$.

In Fig. 2a the temperatures of hot air in a furnace determined by electrostrictive LIGs are plotted vs. the thermocouple values. Each measured value has been averaged over 100 laser shots. For clarity, a dotted line indicating equal temperatures for each method is also shown in the graph. Typically, the standard deviation of the measured oscillation periods is 0.5%. Such an accuracy is obtained by a straightforward determination of the positions of the oscillation peaks. With increasing temperature a decreased gas density, together with increased values of thermal conductivity and viscosity, leads to a reduction in signal strength. Additionally, fewer peaks of the temporal evolution of the electrostrictive LIG signal
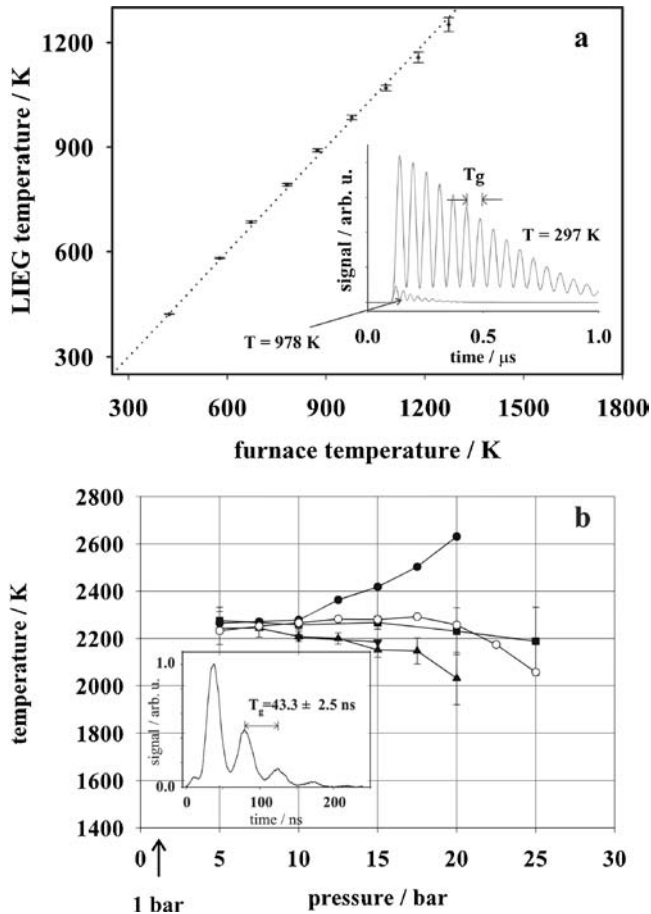
FIGURE 2 **a** Temperature measurement in air at atmospheric pressure by an electrostrictive LIG vs. temperature measurement by a thermocouple inside a furnace. The signal is averaged over 100 shots. The *dotted line* corresponds to an equality of the temperature measurements. *Inset*: temporal evolution of the electrostrictive LIG signal in ambient air at temperatures of 297 K (*upper trace*) and 978 K (*lower trace*). The signals are averaged over 100 shots. **b** Temperature measurements in the post-flame gases of a premixed methane/air flame obtained by thermal LIGs, recorded at different days and by CARS (*open circles*) vs. pressure. *Inset*: temporal behavior of a thermal grating obtained in a stoichiometric CH_4/air flame at atmospheric pressure. The height above the burner surface is 2 mm. The signal is averaged over 100 laser shots. From the measured oscillation period of the signal a temperature of 2080 ± 245 K is determined

are observed due to the enhanced damping of the acoustic wave. This effect is illustrated in the inset of Fig. 2a, which shows an example of the temporal evolution of the diffraction efficiency of an electrostrictive LIG recorded in air at atmospheric pressure for two different temperatures. Both traces have been normalized to their respective maxima. At higher temperature, the lower density leads to a stronger damping of the acoustic wave and to a smaller signal strength. In addition, an increased sound velocity at higher temperature results in a shorter oscillation period as well as in a shorter residence time of the acoustic waves in the probe volume. As a consequence, a faster decay of the grating diffraction efficiency is observed. The standard deviation for the determined oscillation period is therefore larger and gives rise to an increased error for the temperature measurement. There is good agreement, within the error bars, between the temperature determined by the laser-induced-gratings method and the thermocouple readings.

To estimate the statistical error of single-shot temperature measurements by the electrostrictive LIG method, a number of single-shot measurements have been carried out at a fixed furnace temperature of 1376 K (reading of the thermocouple). A number of 100 single-shot measurements is considered to be a good basis for a statistical analysis. The measured temperatures have been compiled in a normalized histogram with a bin width of 10 K. From the measurements, a mean temperature of 1370 K with a standard deviation of 72 K is deduced. The data have been fitted with a Gaussian probability function. The width of the distribution essentially reflects the uncertainty of the measurement. The consistency with the Gaussian distribution implies that random processes are responsible for the observed fluctuation in the derived temperatures. Owing to the limited photon flux these fluctuations may arise from the photoelectron statistics and the quantization noise of the digitizer.

Finally, the method has been applied for thermometry of premixed methane/air flames in a high-pressure burner described in detail in Ref. [33]. To validate the temperature measurements by the LIG method, CARS thermometry has been performed simultaneously in the post-flame region. The results are depicted in Fig. 2b where four independent temperature vs. pressure curves by LIG, and one by CARS, are shown. The flames have been stabilized in a pressure range between 1 and 25 bar on a water-cooled sinter plate of 20-mm diameter. Gas velocity and mixture composition have been adjusted by mass-flow controllers, and mixing ratios λ (air to fuel ratio) varied between 0.5 and 1.3. Up to pressures of 10 bar a fairly good agreement between the temperatures obtained by CARS and by the laser-induced-grating method has been observed. Every measurement sequence has been recorded at a different day. At increased pressures the flame in the high-pressure burner becomes unstable (turbulent) and the temperatures determined with the two methods differ drastically. The reason for this discrepancy and the bad reproducibility of the LIG temperatures are at present unclear and need to be investigated in more detail in the future. Beam-steering effects resulting in a shot-to-shot variation of the intersection angle of the excitation beams might be pronounced at higher pressures, this being an explanation for such a disagreement. Moreover, the small diameter of the flame cone in addition to the limited spatial resolution of the LIG technique may have affected the temperature evaluation. The inset in Fig. 2b shows the temporal evolution of the grating diffraction efficiency obtained in the post-flame region of a laminar premixed stoichiometric methane/air flame at atmospheric pressure stabilized on a flat-flame burner (McKenna). The diameter of the water-cooled, sintered stainless steel flame holder is 50 mm. Depending on the parameters to be measured, different fuels and oxidizers have been used. Although the signal intensity has been averaged over 100 laser pulses, its signature still exhibits distortions because of the limited photon flux. The determined oscillation period of the grating diffraction efficiency is 43.3 ± 2.5 ns. The small peak at the beginning of the signal disagrees with the determined period and cannot be attributed to scattered light from the Nd:YAG laser. Using Eq. (1) with $f = 2$ for an electrostrictive grating and taking into account the gas composition which is known from equilibrium calculations, the measured oscillation period results in

a temperature of roughly 580 K. However, 2065 ± 50 K is the established temperature value for a stoichiometric methane/air flame at atmospheric pressure [34]. This significant discrepancy in addition to the appearance of the small peak at the beginning of the signal suggests that a thermal LIG has been formed in the flame due to absorption of the excitation radiation. In this case a value of $f = 1$ in Eq. (1) yields a more realistic flame temperature of 2080 ± 245 K. Likewise, we observed for a stoichiometric hydrogen/air flame that $f = 1$ also results in a realistic value of the flame temperature. The most probable species absorbing the fundamental wavelength of the Nd:YAG laser in the investigated flames are H_2O and OH. A search through the database of HITRAN [35] containing a file with a transition of water vapor at 1500 K delivered four absorption lines of H_2O within the spectral bandwidth of the Nd:YAG laser. The assumption of a thermal grating signal generated by H_2O hot band absorption has been substantiated by a measurement in a premixed laminar CO/O_2 flame stabilized on a flat-flame burner. We observe a oscillation period of 23 ± 1.3 ns. The local gas composition in the measurement volume is estimated from a one-dimensional freely propagating flame calculation and provides the major species mole fractions of $x_{CO_2} = 0.39$, $x_{CO} = 0.37$, and $x_{O_2} = 0.15$. From the oscillation period of the signal and the gas composition from the model, a temperature of 2215 ± 240 K is obtained by setting $f = 2$ in Eq. (1). This result agrees satisfactorily with the adiabatic flame temperature of 2460 K obtained from the calculation, in particular since the model did not account for the heat conduction from the flame to the burner surface leading to a lower adiabatic flame temperature. Thus, we conclude from the measured and calculated temperatures that the nature of the signal recorded in a CO/O_2 flame is purely electrostrictive. It is important to notice that the nature of the generated grating is not clear *a priori*. However, the significant difference in the determined temperatures obtained for different values of f and a consideration of the coincidences with resonant molecular transitions at the excitation wavelength will remove ambiguities in most cases.

2.2   *Concentration measurements*

Electrostrictive LIGs are applicable for concentration measurements of binary mixtures of known temperature. There are two possible strategies to perform such a measurement. The first approach is based on intensity measurements. Since every individual gas has a specific electrostrictive constant, the total signal intensity obtained in a mixture will depend on the relative concentrations of the components. Unfortunately, absolute intensity measurements are difficult to achieve due to significant intensity fluctuations of the excitation and read-out lasers affecting the signal. To account for the effect quantitatively, it is necessary to simultaneously record the intensities of the three input beams and normalize the signal accordingly for each observation. Furthermore, the temporal evolution of the signal has to be modeled carefully to include the effects of viscosity and heat conduction. The second approach is based on sound-velocity measurements. In fact, the sound velocity and thereby the oscillation period of the electrostrictive LIG diffraction efficiency depends on the

gas composition (see Eqs. (1) and (2)). For a binary mixture Eq. (3) simplifies to

$$M = x_1 M_1 + (1 - x_1) M_2, \tag{3'}$$

where x_1 is the mole fraction of the first species. Using Eqs. (2) and (3'), and computing Eq. (4) for two species, it is possible to determine the concentration x_1 for known temperatures of the mixture. To evaluate the performance of this technique, measurements of binary mixtures in a cell at room temperature have been carried out by applying the same experimental setup used for thermometry; see Sect. 2.1. Mixtures of methane/nitrogen and hydrogen/nitrogen are investigated as they represent models for two commonly used fuel/oxidant combinations. Since the electrostrictive response in oxygen and nitrogen is similar, nitrogen has been preferred in all experiments for safety reasons.

In Fig. 3 the oscillation period of the electrostrictive LIG diffraction efficiency is plotted vs. the methane mole fraction (circles) and the hydrogen mole fraction (squares), respectively. The oscillation periods have been obtained from the measurement of the temporal evolution of the grating's diffraction efficiencies. As mentioned above, a period is determined by measuring the maximum position of each peak. Every measurement is an average of 100 laser shots. Increasing the fuel mole fraction results in a decrease of the determined oscillation period corresponding to an increased sound velocity until the sound velocity in pure fuel is obtained. The dashed lines in Fig. 3 are calculated using Eqs. (1)–(3) and employing the oscillation period measured in pure nitrogen as a reference. The effective values of the molar mass and of molar heat capacities are calculated from the corresponding values of the gas-mixture components. As shown in
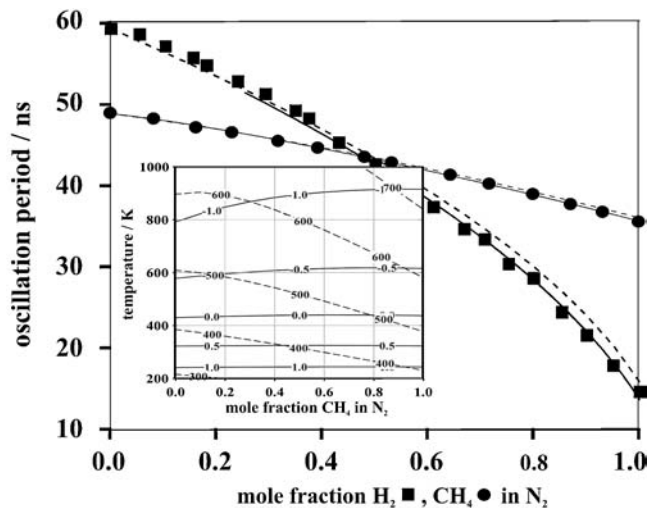
FIGURE 3   Oscillation period of the diffraction efficiency of an electrostrictive LIG measured at 1 bar total pressure and room temperature in a methane/nitrogen mixture (*circles*) and in a hydrogen/nitrogen mixture (*squares*). The *dashed lines* are the theoretical curves based on a calculation. The *solid lines* are a polynomial fit to the measured oscillation periods. *Inset*: plot of the temperature vs. mole fraction of methane in nitrogen for constant sound velocities and logarithm of the grating decay time. The *dashed lines* are the contours of the sound velocities in m/s. The *solid lines* are the contours of the parameter ε, which is defined as $\varepsilon = \ln(\bar{\tau})$, where $\bar{\tau}$ is the decay time in μs. For the calculation atmospheric pressure and a grating fringe spacing $\Lambda = 30$ μm were assumed

Fig. 3, good agreement between calculation and measurement is found, especially for low mole fractions of fuel in N_2. The small systematic difference which increases with increasing fuel mole fraction is probably caused by the dispersion of the sound velocity that may take place in methane and hydrogen. The solid lines in Fig. 3 are obtained by a polynomial fit to the measured oscillation periods. The slope of the curve increases with increasing fuel mole fraction. At a value $x_{CH_4} = 0.5$ the slope is 13.5 ns. The standard deviation of the measured oscillation period is about 0.5%. This uncertainty limits the detection sensitivity for the variation of the gas composition in a 1:1 mixture of methane and nitrogen to 2%. The detection sensitivity increases for large sound-velocity differences of the mixture components, which is the case for the hydrogen/nitrogen mixture. At $x_{H_2} = 0.5$ mole fraction, the slope is 40 ns. This translates to a minimum detectable concentration variation of the gas-composition value of 0.6% for a 1:1 mixture of hydrogen and nitrogen. In almost pure hydrogen the detection limit for nitrogen is about 0.1%.

To estimate the statistical error of a single-shot concentration measurement, about 60 single-shot signals have been recorded in a mixture of a 0.55 mole fraction of methane in nitrogen. The measured oscillation periods have been compiled in a normalized histogram with a bin width of 0.1 ns. The distribution of the measured oscillation period is fitted by a Gaussian probability density function, resulting in a well-defined maximum at 44.1 ns with a width (FWHM) of less than 0.2 ns.

By simultaneous measurements of the oscillation period and of the signal decay due to acoustic damping, both concentration and temperature are accessible at once if the acoustic transit time τ_{tr} fulfills the relation $\tau_{tr} > \tilde{\tau}$, where $\tilde{\tau} = (2\beta_1)^{-1}$ is the acoustic decay time and β_1 is the decay rate; see Eq. (19) of Ref. [1]. The inset of Fig. 3 shows a plot of the temperature vs. the mole fraction of methane in nitrogen for different values of sound velocities and of the parameter ε, which is defined as $\varepsilon = \ln(\tilde{\tau})$, where $\tilde{\tau}$ is expressed in μs. The contours of the sound velocity (dashed lines) are plotted for 300 m/s, 400 m/s, 500 m/s, and 600 m/s and have been obtained using Eqs. (2), (3'), and (4). The solid lines represent the contours of the parameter ε for the values between -1 and $+1$, with a step of 0.5. These contours have been obtained with a grating spacing $\Lambda = 30\,\mu$m and by using the tabulated values of the viscosity η_{visc}, the thermal conductivity κ, and the heat capacities at constant pressure and volume c_P and c_V [51] to calculate the density at the corresponding temperatures at the pressure of 1 bar; see Eq. (19) of Ref. [1]. For temperature values below 600 K the decay time remains nearly constant for all concentrations. Consider for example the trace of the parameter $\varepsilon = 0$ that corresponds to a decay time of 1 μs. For this decay time the possible temperatures are in the range between 430 K and 450 K. If in addition a sound velocity of 500 m/s is measured, then the range for the possible concentrations of methane in air lies between 0.79 and 0.83. Thus, for binary mixtures the method is applicable to determine simultaneously a range for the concentration and the temperature.

So far we have described the method of electrostrictive LIGs for concentration measurements. In the following, the application of thermal LIGs as a highly sensitive tool for concentration measurements of trace species is presented.

Conventionally, laser-induced fluorescence (LIF) or Raman scattering would be the method of choice for concentration measurements. However the Raman effect is extremely weak. Hence, only species concentrations above 1% are generally accessible. Laser-induced fluorescence exhibits a high sensitivity but relies on an adequate transition with a high fluorescence quantum yield. Furthermore, due to quenching, absolute concentration measurements are not performed in a straightforward manner for most species. In the following we discuss the high sensitivity of the LIG technique and propose the method as a complementary tool to LIF for concentration measurements. Thermal LIGs are especially suited for detection of species with a low fluorescence quantum yield. Note, however, that strong quenching is required to obtain a high sensitivity. In addition, the dependence of the temporal shape of the LIG signal on temperature, pressure, and gas composition has to be known in detail for quantitative measurements. Nevertheless, an illustration of the excellent sensitivity of the LIG method is given by Cummings [36]. In this study thermal gratings are excited in room air by tuning the wavelength of the laser to an absorption line of NO_2. Because NO_2 is present in ambient air at trace-level concentration only, the sensitivity of the grating method has been estimated to be better than 50 ppb.

The thermal LIG signal is strongly enhanced by adding an efficient quencher to the sample. Based on this idea, thermal LIGs have been applied in our laboratory to detect the isotopic molecule $^{16}O^{18}O$ at the natural abundance of 0.4%. The details can be found in Ref. [3], while here the results are briefly summarized. The transition moments of the lines belonging to the $b^1\Sigma_g^+ \leftarrow X^3\Sigma_g^-$ electronic system of oxygen are small. Neither laser-induced fluorescence nor laser-induced gratings are sufficiently efficient to detect oxygen at the wavelength range of the excitation laser (see below). However, adding some water vapor to the sample of pure oxygen enhances the thermal grating signal by several orders of magnitude. To demonstrate the effect, a partial pressure of 0.018 bar of water has been added to an oxygen sample at 1 bar, which corresponds to the vapor pressure of air at room temperature. This sample has been scanned for lines of the isotopic molecule $^{16}O^{18}O$ occurring in natural O_2. The transition frequencies in $^{16}O^{18}O$ are shifted to higher frequencies compared to the frequencies in $^{16}O_2$. The experimental setup used for this investigation is briefly described in the following (for details see Ref. [3]). The grating excitation beams are obtained from a single-longitudinal-mode optical parametric oscillator (Continuum HRL-100Z). Its pulse length is about 5 ns and its bandwidth is specified to be smaller than 500 MHz. Focused by a lens ($f = 1000$ mm), the two excitation beams intersect at their focus, which is located in a sample cell. At this point the total intensity is roughly 10 GW/cm². The crossing angle θ between the two excitation beams is set to about 1°. A second lens ($f = 1000$ mm) has been used to direct the probe beam arising from a cw Ar^+ laser (Coherent Innova 70-4) running in a single-line mode at $\lambda_{pr} = 514.5$ nm. The three beams have been arranged in a planar backward phase matching geometry. Oxygen with a purity of 99.5% has been used for all measurements and no special care has been taken to remove residual water from the gas or the sample cell.
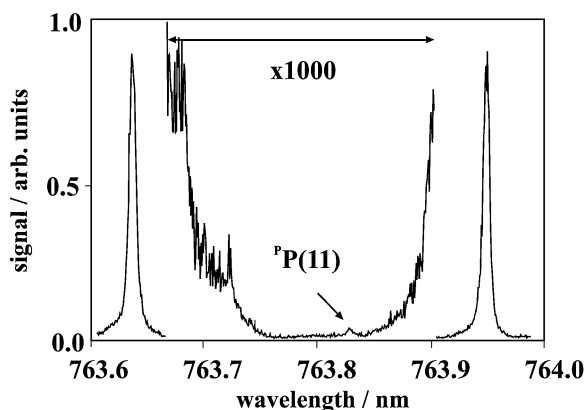
FIGURE 4   Part of the grating spectrum obtained in a mixture of 1 bar O_2 and 0.018 bar H_2O. For the middle part of the spectrum, the signal-detection sensitivity is enhanced by a factor of 1000. The transition $^PP(11)$ of the 0-0 band in the red system of $^{16}O^{18}O$ is marked

Synchronously to the recording of the laser-induced spectrum, the laser power has been monitored. In addition, an absorption spectrum over a path length of 10 m has been recorded in a cell containing pure oxygen at 1 bar and ambient temperature. In the spectral range 765.6 nm to 763.8 nm, the transitions $^PP(17)$, $^PP(15)$, $^PP(13)$, and $^PP(11)$ of the 0-0 band in the $b^1\Sigma_g^+ \leftarrow X^3\Sigma_g^-$ system of $^{16}O^{18}O$ are clearly resolved. Unfortunately, the isotopic lines are masked in large parts of the measured spectral region by the wings of the intense transitions belonging to the homonuclear molecule. Nevertheless, the isotopic $^PP(11)$ line is undoubtedly visible even though its intensity is decreased by a factor of more than 5×10^4 with respect to the neighboring $^PP(9)$ and $^PQ(11)$ lines of the homonuclear molecule (Fig. 4).

2.3   *Investigation of energy-transfer processes and detection of resonant transitions*

Resonant absorption of radiation via one- or two-photon transitions and subsequent exchange of internal energy with the thermal bath by collisions leads to a density variation inside the probe volume. If the density change is rapid, an acoustic wave is formed which can be detected by microphones usually employed in photoacoustic spectroscopy. This technique has been used for a wide variety of chemical-kinetics and energy-transfer investigations [37]. Alternatively, the induced density variation can be detected by observing deflection [38] or change of the shape [39] of a cw probe laser beam. Thermal laser-induced gratings were first employed for investigations of energy-transfer processes after pumping iron(III) tetraphenylporphyrin chloride by Andrews and Hochstrasser [40] more than 20 years ago. Compared to thermal deflection and thermal lensing spectroscopy, the use of thermal gratings has the advantage of a simpler experimental arrangement and an easier interpretation of the obtained results.

In the present section we review our studies published elsewhere [3, 4, 6, 7, 29] of the experimental characterization and qualitative analysis of various LIGs simultaneously excited in molecular gases. All investigations have in common that the LIGs result from resonant excitation of molecules by

absorption (in O_2) or Raman transitions (in CO_2) followed by multistage processes of collisional redistribution of internal energy. In addition, we demonstrate the feasibility of detecting absorption or Raman transitions using LIGs [3, 6, 9]. An assessment is given of the applicability of the LIG technique for investigations of collisional relaxation processes, by an example of quantitative analysis of LIGs observed in neat O_2 [7]. Molecular oxygen was chosen as a test object to observe and study various distinct contributions to the LIG formation. This diatomic molecule has two low-lying metastable singlet states, $b^1\Sigma_g^+$ and $a^1\Delta_g$, that can be rovibronically selectively excited by optical photons. Upon excitation, due to collisions the $b^1\Sigma_g^+$ state can exchange the electronic and vibrational energy with the $a^1\Delta_g$ state ($E-E$, V, T relaxation), while the $a^1\Delta_g$ state can transfer the vibronic energy to the vibrational one in the ground electronic state (intersystem crossing, or $E-V$, T relaxation). For processes involving different electronic states, rotational ($R-T$) and vibrational ($V-V$ and $V-T$) relaxation within one electronic state occur in parallel. A variety of the collisional relaxation processes is characterized by rates that differ by orders of magnitude. Hence, these processes can be separated experimentally by changing gas density. Since O_2 properties are of importance for both fundamental knowledge and various applications in physics, astrophysics, chemistry, and biology, they have been thoroughly studied by different methods, and numerous data concerning the rovibronic energy structure, spectroscopy, relaxation pathways, and corresponding rate constants for O_2 molecules in various environments can be found in the literature.

In our studies LIGs were created via selective excitation of weak magnetic-dipole rovibronic transitions of the 0-0 band in the $b^1\Sigma_g^+ \leftarrow X^3\Sigma_g^-$ system. Figure 5a shows the temporal behavior of the diffraction efficiency of a grating generated by a single pulse of the excitation laser, tuned to the $^PP(9)$ line in the 0-0 band, in a mixture of 1 bar oxygen and 0.05 bar carbon dioxide at room temperature. CO_2 is an efficient quencher for O_2 in the $b^1\Sigma_g^+$ state and has been added because the self-quenching efficiency of O_2 is four orders of magnitude lower [41]. The signal starts with a sharp peak coincident in time with the grating excitation pulse (see inset of Fig. 5a). It has a leading edge with a duration of about 5 ns and does not match the periodicity of the subsequent part of the signal. A correct description of the observed temporal evolution of the LIG diffraction efficiency is obtained by taking into account the contribution from the induced population change of O_2 molecules (population LIG) (see Ref. [7] for details). The appearance of the oscillating part of the signal is mainly determined by a superposition of a population and an instantaneous thermal contribution, while the electrostrictive contribution is insignificant [1]. After the oscillating part has vanished, because the acoustic waves have left the interaction volume, rather than because of damping, the signal passes through the observable minimum (see Fig. 5a). After some delay, a broad unstructured hump appears.

To qualitatively describe the observed time evolution of the LIG diffraction efficiency, a three-stage model for the energy exchange was assumed. At the first stage, the redistribution of population of the rotational levels within the ensembles of
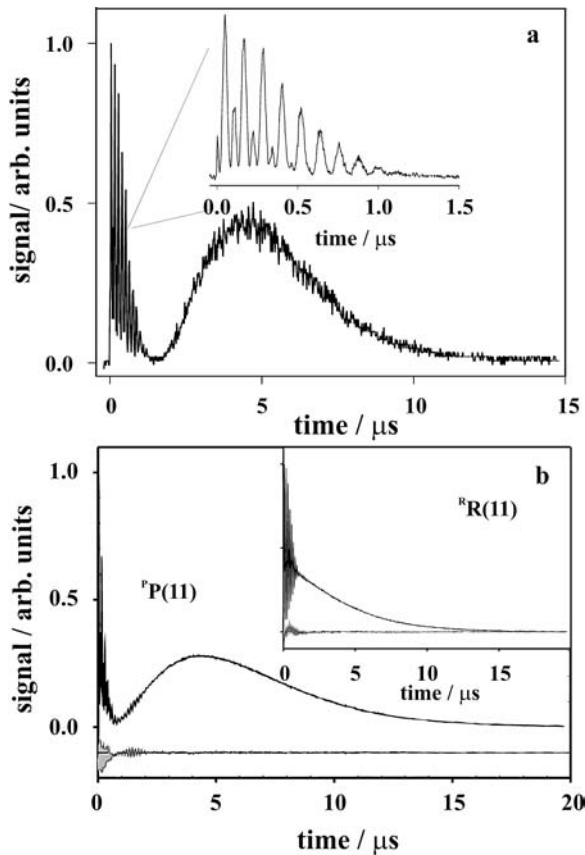
FIGURE 5 **a** Single-pulse laser-induced thermal grating signal obtained in a mixture of 1 bar O_2 and 0.05 bar CO_2 generated by tuning the excitation laser to the $^PP(9)$ line in the 0-0 band in the $b^1\Sigma_g^+ \leftarrow X^3\Sigma_g^-$ system of oxygen. *Inset*: first part of the signal at higher temporal resolution. **b** Thermal grating signal obtained in 2 bar pure O_2 at room temperature by pumping $^PP(11)$ of the 0-0 band of the red system of oxygen. *Inset*: pumping $^RR(11)$ of the 0-0 band of the red system of oxygen

the excited and ground-state molecules follows the excitation process. This redistribution occurs practically instantaneously and leads to the generation of acoustic waves and a stationary density modulation. The time constant for quenching of oxygen in the $b^1\Sigma_g^+$ ($v' = 0$) state in a mixture of 1 bar oxygen and 0.05 bar carbon dioxide is 1.9 µs (see Ref. [4]). This is too slow to excite an acoustic wave contribution that is comparable to the one excited by rotational relaxation. The internal energy conversion to (or from) translational energy, which accompanies R–T relaxation, occurs almost instantaneously and can thus generate a stronger oscillating signal (see Eq. (22) of Ref. [1]). Note that R–T relaxation upon excitation of the P-branch transitions is an endothermic process and results in spatially modulated cooling of the gas. As a consequence, the population and the instantaneous thermal contributions have opposite signs.

The second stage is governed by a slower electronic quenching of the $b^1\Sigma_g^+$ state (E–E, V, T relaxation) by CO_2 and results in the appearance of vibrationally excited $O_2(^1\Delta_g)$ and CO_2 (see Ref. [41]). The minimum observed in the signal strength at this stage (Fig. 5a) is accounted for by the destructive interference of stationary density modulations created by endothermic rotational relaxation and exothermic quenching having opposite signs.

At the last stage, the vibrational energy of CO_2 and O_2 is converted into translational energy in the course of V–V and V–T relaxation. According to this model, the relatively slow energy release during the second and the third stages accounts exclusively for the generation of a stationary density modulation. This modulation manifests itself as the broad unstructured hump and decays by heat conduction (Fig. 5a) at roughly 5 µs.

In neat O_2, manifestations of the same collisional relaxation processes in the temporal behavior of the LIG diffraction efficiency can be observed at higher pressures. Figure 5b depicts the LIG signals obtained in 2 bar O_2 at room temperature. By exciting the $^PP(11)$ transition of the 0-0 band in the $b^1\Sigma_g^+ \leftarrow X^3\Sigma_g^-$ system, the oscillating part of the signal, due to instantaneous energy exchange, is found to be separated from the non-oscillating part, caused by slow quenching of the $b^1\Sigma_g^+$ state in neat O_2. The pronounced minimum in the signal strength between these two contributions, similar to that observed in the mixture with CO_2, is again a consequence of the difference in signs of the population and the two thermal (endothermic and exothermic) LIG contributions involved. If the R-branch transitions of the 0-0 band are excited, rotational relaxation becomes an exothermic process, and this changes the shape of the signal temporal evolution (see inset of Fig. 5b, with the $^RR(11)$ transition used for LIG excitation).

The temporal evolution of the LIG signals in neat O_2 presented in Fig. 5b was quantitatively described using relations similar to Eqs. (14), (15), and (17) of Ref. [7]. The difference of experimental and fitted traces is shown in the lower part of each plot. By using the electrostrictive contribution as an internal standard, the population grating contribution and the amount of energy exchanged at each stage of the relaxation process can be determined. The results show that the obtained values of the exchanged energies agree fairly well with calculations taking into account the line strengths of the rovibronic transitions and spectroscopic and transport parameters of O_2 [6, 7].

The feasibility of highly sensitive detection of weak absorption transitions using the LIG technique, by recording the signal strength while tuning the wavelength of the excitation laser, was demonstrated in neat oxygen at a pressure of 1 bar. Wavelength scans, covering the spectral range of the ^RR and the ^RQ branches of the 0-0 band in the $b^1\Sigma_g^+ \leftarrow X^3\Sigma_g^-$ system, were performed. Two distinct time intervals were used for the signal integration. The first interval started 20 ns before the excitation pulses and lasted 470 ns, and hence covered most of the oscillatory part of the signal. The second interval started 3.45 µs after occurrence of the excitation pulses and ended 100 ns later, and thus captured the maximum of the unstructured component of the signal. Figure 6 shows the spectrum derived from the oscillatory part of the LIG signal (middle trace) in the wavelength range 759.7–761.7 nm together with the simultaneously recorded absorption spectrum (upper trace). The lower trace in Fig. 6 depicts the spectrum derived from the non-oscillatory part of the signal. The spectra were normalized to the laser power, and a Gaussian with a FWHM of 0.02 cm^{-1} was employed as numerical filter of the single-shot data. All the lines were identified using the line positions measured by Babcock and Herzberg [42]. The line positions in the absorption spectrum and in the LIG
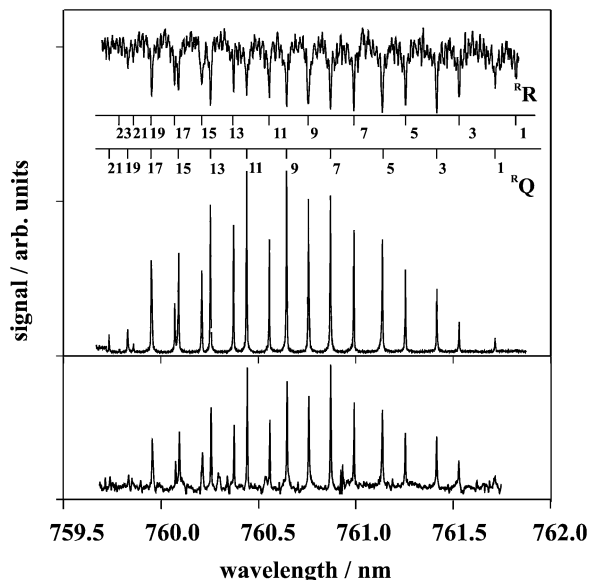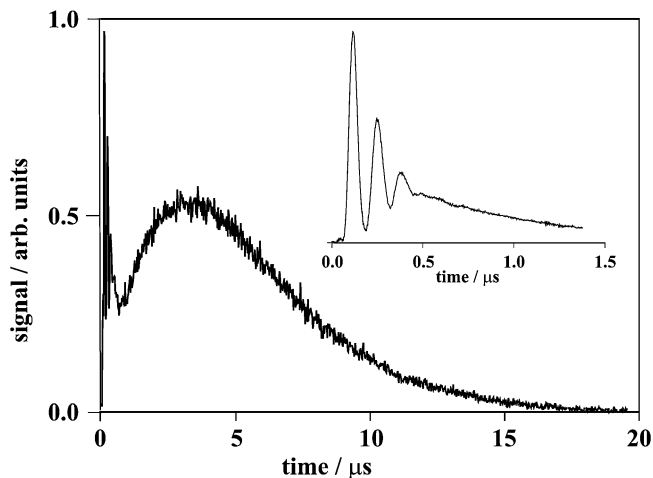
FIGURE 6 Wavelength scan of the excitation laser in pure oxygen at 1 bar in the 0-0 band of the $b^1\Sigma_g^+ \leftarrow X^3\Sigma_g^-$ system. Absorption spectrum (*upper trace*) and spectrum derived from the oscillating part of the LIG signal (*middle trace*). Spectrum derived from the unstructured part of the grating signal (*lower trace*)

FIGURE 7 Single pulse of a Raman-excited thermal grating signal obtained in a mixture of 0.1 bar CO_2 and 1.9 bar Ar at room temperature. The excitation is resonant with the ν_1 Q-branch. *Inset*: single pulse of a Raman-excited thermal grating signal obtained in 0.2 bar CO_2 at room temperature. The excitation is resonant with the ν_1 Q-branch

spectra derived from the oscillatory and the non-oscillatory parts of the signal agree within the measurement accuracy of $\pm 0.01\,\text{cm}^{-1}$. The resonant contribution to the oscillatory part of the signal is a few tens of times stronger than the non-resonant electrostrictive contribution, which appears as a constant background in the corresponding LIG excitation spectrum. The spectrum derived from the non-oscillatory part of the LIG signal is free of any background. However, due to the low self-quenching efficiency of oxygen in the $b^1\Sigma_g^+$ state, this signal is about 30 times smaller than that of the oscillatory part and hence shows a rather poor signal-to-noise ratio. The measured line widths of $0.1\,\text{cm}^{-1}$ (FWHM) in the absorption spectra agree with literature values [43] and are mainly attributed to pressure broadening. The LIG excitations spectra have smaller line widths of about $0.07\,\text{cm}^{-1}$ (FWHM).

It is not always possible to find a dipole-allowed transition in the spectral range conveniently accessible by lasers. Therefore, there is an interest to excite species via two-photon Raman transitions in order to generate thermal LIGs. Such gratings can be created by spatially and temporally overlapping the interference pattern produced by one laser with the beam of a second, tunable, laser, that differs in its frequency from the first by a Raman frequency of the medium. On the other hand, overlapping two interference patterns formed independently by these two lasers can enhance the contrast of the grating. The required experimental setup is slightly more complex [4, 29] than those used for studies employing non-resonant or one-photon-excited LIGs. Note that the experimental configuration we employed allowed us, using the same excitation lasers, to observe CARS signals from the species of interest simultaneously with Raman-excited LIG signals. Thus, the efficiency of LIG generation was controlled while tuning the laser frequency.

To demonstrate the feasibility of Raman excitation of thermal LIGs and for further investigations of relaxation pro-

cesses, CO_2 was chosen. This selection was guided, first, by the presence of two strong and narrow Q-branches of Raman-active rovibrational transitions (ν_1 and $2\nu_2$ bands) that could be efficiently excited by the available lasers and, second, by the possibility of generating a variety of LIGs in a wide range of gas densities and to observe collisional energy exchange processes at different time scales. This possibility is ensured by sufficiently large amount of data available on vibrational energy levels of CO_2 and their collisional relaxation rates. Note that it also eases the interpretation of the results.

In Fig. 7 a manifestation of the slow release of absorbed laser energy is shown. The depicted temporal behavior of the diffraction efficiency was recorded at a Raman resonance in a mixture of 0.1 bar CO_2 and 1.9 bar argon. The slow release of absorbed laser energy contributes to the development of a stationary density modulation only. It is observed as a maximum in the temporal evolution of the LIG signal at about $3.5\,\mu\text{s}$ after occurrence of the laser pulses setting up the grating. The inset of Fig. 7 depicts the temporal evolution of a grating signal that was obtained in 0.2 bar CO_2 by exciting the rovibrational transitions of the ν_1 Q-branch. The density variation in the form of acoustic waves, due to rapid release of a part of the absorbed excitation energy in the form of heat, is observed to exceed that generated by electrostriction. The contribution from electrostriction to the LIG diffraction efficiency is recognizable as a small peak at the beginning of the temporal development of the LIG signal. The stationary density modulation persists longer in the excitation area than the acoustic waves and leads to the extended unstructured tail of the signal.

Electrostriction and fast energy exchange between the laser-excited 10^00 or 02^00 level of CO_2 and the thermal bath characterize the early phase ($t = 0$–$400\,\text{ns}$) in the observed temporal evolution of the LIG diffraction efficiency. The energy exchange takes place during the redistribution of population within the multiplet of vibrational states $\{10^00, 02^00, 02^20\}$ due to collisions with CO_2 in the ground state or with Ar atoms (V–V', T relaxation). At room temperature and a

pressure of 0.2 bar, transitions from the vibrational state 10^00 or 02^00 to 02^20 occur in 9–15 ns [44]. Likewise fast is the vibration–vibration $(V-V, T)$ relaxation of CO_2 (02^20) by collisions with CO_2 in the ground state, yielding CO_2 in the vibrational state 01^10 [44]. If buffer gas is added, these processes take place significantly faster. Subsequent vibration–translation $(V-T)$ relaxation is very slow. For CO_2 and Ar as collision partners the time constants of relaxation are 38 μs (0.2 bar CO_2) and 22 μs (0.1 bar CO_2 and 1.9 bar Ar), respectively [45, 46]. Therefore, it is $V-T$ relaxation of CO_2 (01^10) that primarily maintains the formation of a stationary density modulation late in the temporal evolution of the diffraction efficiency (see Fig. 7). Molecular diffusion washes out the spatial density modulation of molecules in the excited state and controls the amount to which the relatively slow $V-T$ relaxation contributes to the formation of a stationary density modulation. Moreover, the previously generated temperature variation is destroyed by heat conduction. Adding buffer gas slows down the diffusion of excited CO_2 molecules and maintains spatially modulated release of the excited-state energy. Furthermore, heat conduction in the mixture is reduced. Hence, strength and duration of a LIG signal are strongly enlarged at higher gas densities. All these variations of LIGs' temporal evolution are described using modeling equations presented in Sect. 2 of Ref. [1] and by fitting experimental data. It should be noted that at the excitation of distinct molecular levels the relaxation pathways and the amounts of exchanged energies are usually different and lead to differences in the temporal evolution of LIG diffraction efficiency.

LIG excitation spectra of Raman resonances in CO_2 were recorded in a similar way as was described above for O_2. The spectra depicted in Fig. 8 were obtained for the $2\nu_2$ Q-branch at 1 bar of pure CO_2. Again, two distinct time intervals were employed for signal integration. A relatively narrow time gate (width 130 ns) was used in the early phase of the LIG signal, which is dominated by the density oscillation. The noticeable background is due to the electrostrictive contribution. A second time gate (width 3 μs), centered 3 μs after the occurrence

FIGURE 8 Spectra of the $2\nu_2$ Q-branch obtained in 1 bar CO_2 by integrating the oscillating part of the signal. *Inset*: signal obtained by integrating the part of the signal resulting from the stationary density modulation

of the excitation pulses, captured the maximum of the signal caused by the stationary density modulation, and provided a background-free spectrum; see inset of Fig. 8.
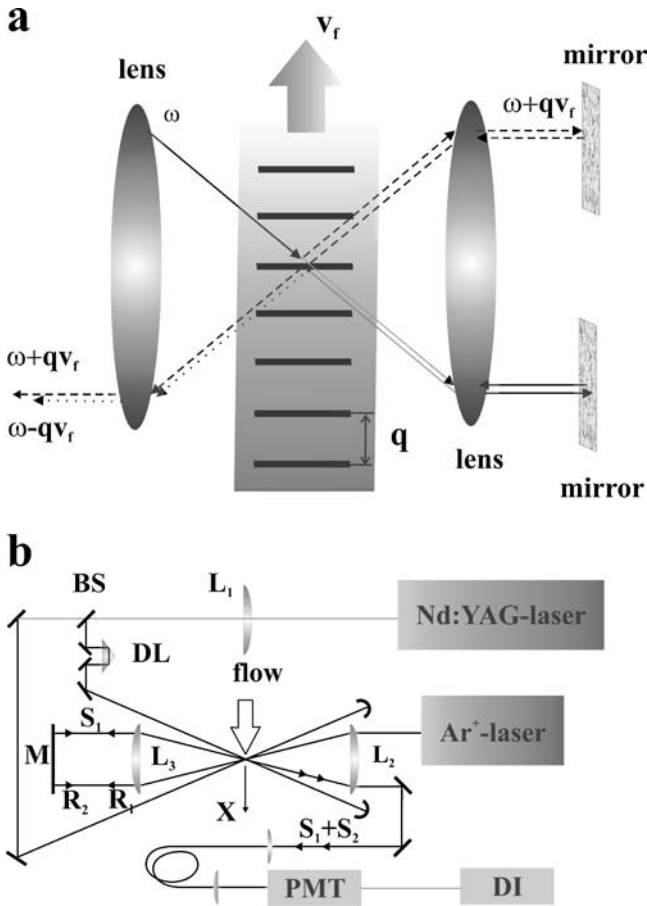
2.4   *Flow-velocity measurements*

Flow velocity and temperature are key parameters for the characterization of aerodynamic and reacting flows. While there is a variety of dedicated techniques available to determine one of these two parameters, there are few attempts to measure both simultaneously. Well-established methods to measure flow velocities rely on seeding the flow with particles and thus do not allow a non-intrusive measurement, e.g. laser Doppler anemometry (LDA), particle-imaging velocimetry (PIV), and Doppler global velocimetry (DGV). Furthermore, due to particle lag, these techniques fail to measure high-velocity flows and flow velocity close to surfaces. Single-shot time-domain coherent anti-Stokes Raman scattering [47] circumvents these problems and allows for simultaneous measurements of temperature and flow velocity. Due to the limitation by the Raman coherence time, this technique is more suited for measurements of high velocity, low-pressure flows. For room-temperature flows the pressure limit is about 0.01 bar. Schlamp et al. [48] demonstrated the possibility of deducing flow velocities by analyzing the temporal shape of a signal originating from a thermal grating generated by using a misaligned beam geometry. Walker et al. [49] employed the Doppler shift experienced by a laser beam diffracted by a thermal grating. The authors used the frequency rather than the time domain to determine flow velocities. Decay analysis of laser-induced electrostrictive gratings as well as a time-of-flight approach have been proposed by Ribet and Lefebvre [50] for flow-velocity measurements.

In the following, an overview of the results of Refs. [27] and [28] is presented. In these works it has been demonstrated for the first time to the authors' knowledge that laser-induced electrostrictive gratings can be applied to measure flow velocities and temperatures simultaneously. The principle of the method is shown in Fig. 9a. It consists in local 'seeding' of the jet with a laser-induced standing ultrasound wave and the heterodyne detection of light scattered by this wave. If an electrostrictive grating is generated in a flow moving with velocity v_f, the induced density modulations are no longer at rest but will move along with the flow. A probe beam diffracted by such a grating will be frequency shifted. This shift can be interpreted as a Doppler effect due to the movement of the grating. If the grating is read out in the opposite direction to the flow, see upper left hand side of Fig. 9a, the frequency shift is $\Delta\omega = +\mathbf{q}\mathbf{v_f}$, where $\mathbf{q}$ is the grating vector and $\mathbf{v_f}$ is the flow-velocity vector. For a read out of the grating in the opposite direction to the flow as shown in the lower right hand side of Fig. 9a the frequency shift is $\Delta\omega = -\mathbf{q}\mathbf{v_f}$. The frequency shift is given by the velocity component normal to the grating planes and it thus reaches its maximum value when the planes are perpendicular to the flow-velocity vector. The superimposition of these two coherent signal beams on the detector, see lower left hand side of Fig. 9a, results in a total signal which displays a fast oscillation at twice the acoustic frequency modulated by a lower frequency
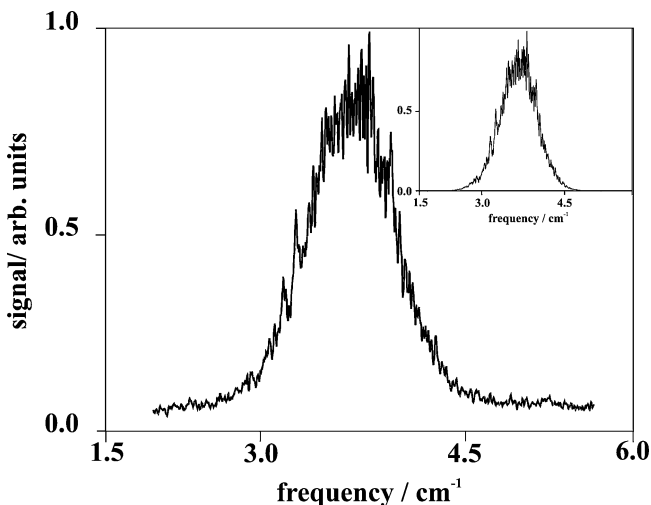
FIGURE 9 **a** Principle of flow-velocity measurement by laser-induced electrostrictive gratings. Two signals generated from reading out the grating in opposite directions are Doppler shifted by $\Delta\omega = \pm \mathbf{q v_f}$ due to the movement of the flow. From the heterodyne detection of the two signals the flow velocity is obtained. **b** Setup for the velocity measurements. BS, beam splitter (50%); L_1, L_2, and L_3, lenses ($f = 1000$ mm); DL, delay line; M, mirror; PMT, photomultiplier tube; DI, digitizer; S_1, S_2, signal beams; R_1, R_2, read-out beams

at $2\mathbf{q v_f}$ (beat frequency) due to the mixing of light of opposite Doppler-shifted frequencies. Therefore, the analysis of the time evolution of the total signal allows us to determine the flow velocity from the beat frequency and the temperature from the acoustic oscillations, as described in Sect. 2.1.

The setup used to perform simultaneous flow-velocity and temperature measurements by LIGs is shown in Fig. 9b; see Ref. [27]. For the excitation beams the fundamental output of a Nd:YAG laser has been used, while the read-out beam has been provided by a cw Ar^+ laser. The two signal beams S_1 and S_2 have been obtained by reading out the grating in opposite directions and thus their Doppler shifts have the same size but opposite signs. Assuming that the time delay Δt between the two signal beams is much smaller than the oscillation period T_g of the grating scattering efficiency and the acoustic decay time $\tilde{\tau} = (2\beta_1)^{-1}$, i.e. $\Delta t \ll T_g, \tilde{\tau}$, one can deduce for the resulting signal impinging on the detector [27]:

$$P_S(t) \propto [1 + m \cos(\Omega_M t + \psi)] \sin^2(\varpi t) \exp(-2\beta_1 t)$$
$$\times \exp(-2(t/\tau_{tr})^2), \tag{6}$$

where $\Omega_M = 2\mathbf{q v_f} = 2(v_f/v_{S_0})\varpi_0$ is   the   modulation   frequency   of   the   signal   due   to   the   flow,

$m = 2A_{S_1} A_{S_2}/(A_{S_1}^2 + A_{S_2}^2)$ is   the   modulation   coefficient of the beats, A_{S_i} is the amplitude of signal beam S_i, and ψ is a phase factor which takes into account the effective shift experienced by signal beam S_1 and read-out beam R_2 traveling on different optical paths to the back-reflecting mirror M. Subscript 0 refers to the reference condition at room temperature. As defined in Sect. 3.4 of Ref. [1], τ_{tr} denotes the acoustic transit time.
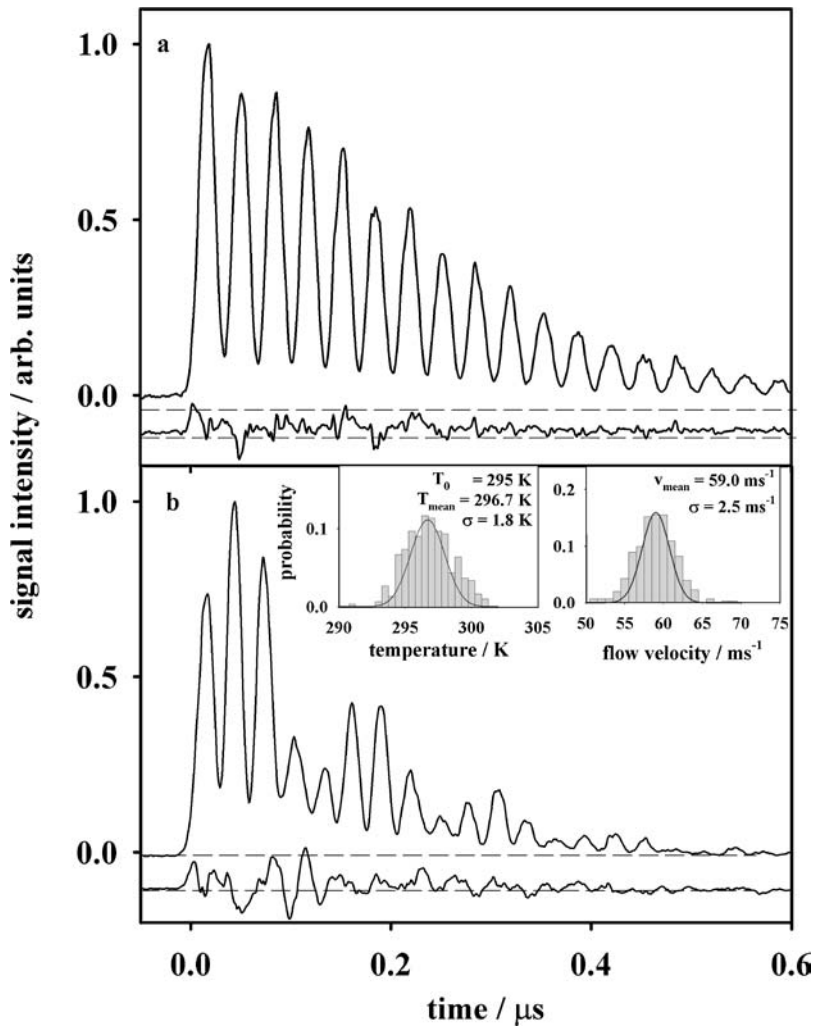
Measurements have been carried out in submerged atmospheric pressure air jets from a slot nozzle in the temperature range from 295 K to 600 K for several flow rates Q between 10 and 200 l/min. The average flow velocity v_Q at the exit of the nozzle is calculated from the flow rates using the equation of continuity. The probe volume was about 0.2 mm in diameter and 10 mm in length. These values define the spatial resolution of our experiment. The probe volume is centered at the axis of the nozzle (or x axis of the laboratory coordinate system), as close as possible to the nozzle exit plane, and has been adjusted to be parallel to the wide side of the slot (or y axis lying in the exit plane of the nozzle). The excitation beams have been directed in the plane of the nozzle (or x–y plane), see inset of Fig. 11. The probe volume has been completely located inside the central part of the jet. The higher spatial resolution in the z direction has been used to measure the velocity profile across the jet, in the x–z plane, with a step of 0.2 mm.

The upper trace in Fig. 10a is the temporal evolution of a signal obtained in air at room temperature ($T_0 = 295$ K) without flow. Each measured data point is averaged over 30 laser shots. The difference between measurement and best fit from Eq. (6) is shown at the same vertical scale as used for the signal. The corresponding zero line for this difference is shifted for clarity.

From the data in Fig. 10a an angular frequency for the acoustic wave $\varpi_0 = 93.3 \pm 0.3$ MHz is obtained. Taking into account the sound velocity in air [51] for the actual pressure as well as the temperature and the determined acoustic oscillation period, one can calculate the intersection angle of the two excitation beams $\theta = 2.63 \pm 0.01°$, which corresponds to a fringe spacing $\Lambda = 23.19 \pm 0.07$ μm. The temporal evolution of the signal obtained in the presence of a heated air flow is shown in Fig. 10b (upper trace). The low-frequency oscillation due to the beating of the two signal contributions of opposite Doppler shifts is clearly visible. Again, the difference between measurement and best fit from Eq. (6) is shown at the same vertical scale as used for the signal. The corresponding zero line for this difference is shifted for clarity.

The flow-temperature value of $T_{th} = 380$ K has been measured by a thermocouple and the averaged flow velocity of $v_Q = 52.8$ m/s has been calculated from the measured flow rate $Q = 80$ l/min and T_{th}. From the best fit the angular frequencies for the acoustic wave of $\varpi = 107.3 \pm 0.3$ MHz and for the beats of $\Omega_M = 49 \pm 0.3$ MHz have been deduced. Assuming that the air composition and the specific heat ratio γ remain unchanged, a temperature $T = 388 \pm 3$ K can be calculated from the measurement of ϖ. The velocity of the flow $v_f = 89.8 \pm 0.6$ m/s is then obtained from the measured angular frequency Ω_M.

Systematic measurements at the axis of the nozzle for various air-flow rates in the range of $Q = 20$ to 200 l/min

show a linear relationship between the flow velocity v_f determined from the beat angular frequency of the signal and the average flow velocity v_Q: $v_f = 1.5 v_Q$. The measured flow velocity is higher than the average flow velocity because of the parabolic-shaped velocity profile of the nozzle, i.e. high velocity of the flow in the center and almost no flow at the boundary. As a consequence, a flow velocity higher than the average flow velocity has been obtained by measuring at the center of the nozzle; see below.

Simultaneous single-shot measurements of flow velocity and temperature have been carried out in an air flow at room temperature ($T_0 = 295$ K) and with a flow rate $Q = 80$ l/min, corresponding to an averaged flow velocity of $v_Q = 41.1$ m/s. In the inset of Fig. 10b, about 300 temperatures and flow velocities have been compiled in two normalized histograms with a bin width of 0.5 K and 1 m/s, respectively. A fitted Gaussian probability density function (solid line), with a correlation coefficient > 0.94, describes the measured distribution quite well. The obtained mean flow velocity is 59.0 ± 2.5 m/s and the mean value for the temperature is 296.7 ± 1.8 K.

As mentioned above, the spatial resolution of the beam geometry has been determined to be about 0.3 mm along the height of the nozzle (z direction) and 10 mm in the y direction. The higher spatial resolution in the z direction has been used to measure the velocity profile across the jet, in the x–z plane, with a step of 0.2 mm (see Fig. 11). The velocity distribution near the nozzle exit plane has a symmetric shape, close to a parabolic one. The velocity $v_f = 56.0 \pm 2.0$ m/s near the axis of the jet, derived at $T_0 = 295$ K and $Q = 80$ l/min, corresponds to the mean value of the single-shot measurements given above, while averaging of the velocities over z within the range -0.75 mm $\leq z \leq +0.75$ mm agrees fairly well with the estimated value $v_Q = 41.1$ m/s. However, the limited spatial resolution in the y direction results in spatially averaged values of the defined flow velocities and temperatures. One way to enhance the spatial resolution of the electrostrictive LIG method while keeping a high accuracy for the determined flow velocity is to increase the angle between the excitation beams. However, this results in a large grating vector and therefore in a shorter lifetime of the grating, since the decay time of the diffraction efficiency of the grating is inversely proportional to the square of the grating vector; see Eq. (19) of Ref. [1]. Another way would be a tighter focusing of the excitation beams. Despite the advantage of an increased diffraction efficiency obtained with tighter focusing, a drawback has to be taken into account. Since the acoustic transit time is proportional to the beam waist, see Eq. (29) of Ref. [1], a shortening of the decay time of the induced LIG occurs and yields a reduced accuracy.
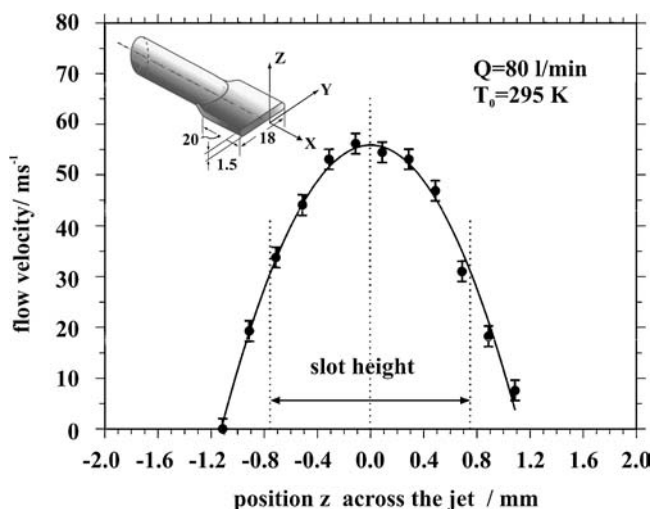
FIGURE 11 Measurement of the jet flow velocities across the height of a nozzle ($v_Q = 32.7$ m/s). The *solid line* is a fit to the data. *Inset*: slot nozzle used for the flow-velocity measurements. It has been manufactured by squeezing one end of a copper tube (dimensions are in mm)

In addition, high temperature and turbulence also shorten the grating lifetime, posing a lower limit to the measurable flow velocity by this method.

Therefore, velocimetry by laser-induced electrostrictive gratings is advantageous for flows exhibiting relatively high density, low degree of turbulence, and high speed. Recently, the authors have used the LIG technique in a modified setup

for the characterization of flows in a large-scale experimental facility–subscale thrust-optimized rocket nozzle [30].

2.5   *Imaging by laser-induced gratings*

One way to map the combustion field is achieved by translating the measurement volume point by point over the region of interest. It is surely a demanding, though an acceptable procedure. Of course it is more convenient and sometimes even necessary (if e.g. the combustion process under investigation is turbulent) to perform a measurement over the entire region of interest simultaneously. Imaging techniques can be incoherent, e.g. laser-induced fluorescence, or coherent, e.g. degenerate four-wave mixing. In this section the imaging potential of laser-induced gratings is reviewed; for details see Ref. [20].

A scheme of the experimental setup used for imaging applications which is very similar to that of Ref. [52] is depicted in Fig. 12. The frequency-doubled output of an injection-seeded Nd:YAG laser (Continuum NY 81-20) operated in single mode has been used to generate all three beams ($\lambda_{exc} = \lambda_{pr} = 532$ nm). The infrared spectral bandwidth of the Nd:YAG laser without any narrowing elements is $1\,cm^{-1}$ and $0.0045\,cm^{-1}$ in single mode by using the injection seeder [53]. It is advantageous to use single-mode operation, since the resulting coherence length of 2 m renders the coherent superposition of the excitation beams without adjustment for equal optical path lengths possible. In fact, by switching the
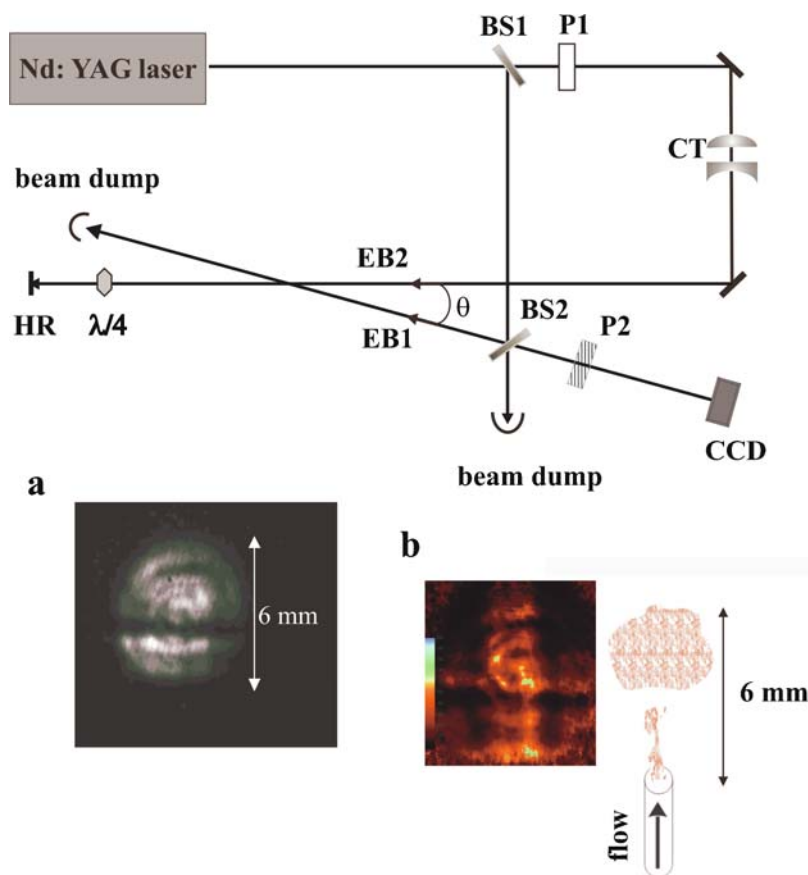

FIGURE 12 Experimental setup for imaging applications by laser-induced gratings. BS1, BS2, beam splitters ($R = 30\%$, 50%, respectively); EB1, EB2, excitation beams; P1, P2, polarizers; CT, cylinder telescope; HR high-reflectivity mirror; CCD camera system. *Inset* **a** Single-shot measurement of ambient air by electrostrictive LIGs. The signal-intensity variations present in this image arise from the inhomogeneities of the intensity profile of the laser beam. The diameter of the displayed spot is approximately 6 mm. *Inset* **b** Single-shot image of a helium jet in air by electrostrictive LIGs. The diameter of the nozzle is about 0.1 mm and the helium pressure difference 0.1 bar. The areas of high helium concentration are displayed *brightly*. The *color scale* is given in arbitrary units. The sketch on the *right-hand side* represents the positions of the nozzle and of the helium flow

Nd:YAG laser from multimode to single-mode operation the electrostrictive signal intensity has been measured to increase by a factor of 180.

To set up the experiment, the output of the laser is split by a 30% reflectivity beam splitter (BS1) into two excitation beams. The weaker excitation beam (EB1) is directed into the interaction region by a 50% beam splitter (BS2) where it crosses the stronger excitation beam (EB2) at an angle θ of about 70 degrees. The beam EB2 is formed into a light sheet about 500-μm thick and 6-mm high by using a Galilean telescope (CT) consisting of two cylindrical lenses. The probe beam is obtained by back reflection of the beam EB2 using a high-reflecting mirror (HR) positioned in the focus of the telescope. For damage-free operation the usable pulse energy on the mirror is limited to 10 mJ. The excitation beam EB2 passes a polarizer (P1) and a $\lambda/4$ plate at the end of the beam path. This combination forms an optical diode protecting the laser from the back-reflected light which is employed as the probe beam. The latter passes the $\lambda/4$ plate twice and is, therefore, perpendicularly polarized to the excitation beams. Optical dumps are used for the excitation beam EB1 past the interaction region and beyond the beam splitter BS2. The two equally polarized excitation beams generate the grating in the medium under investigation and the probe beam is diffracted off the grating. According to the Bragg condition, the signal beam is counter-propagating to the weaker excitation beam. Part of the signal passes the beam splitter BS2 and is detected by an intensified CCD camera (PI CSMA 130). The signal beam exhibits the same polarization as the probe beam and is consequently polarized perpendicularly to the excitation beams. Therefore, stray light mainly arising from the beam splitter BS2 can be efficiently suppressed by using a polarizer P2 in the path of the signal beam. The diffraction efficiency of an electrostrictive LIG generated in ambient air by applying a laser intensity of 90 MW/cm^2 has been measured to be $\eta = (1.5 \pm 0.2) \times 10^{-9}$. As a result, the intensity of the signal beam is sufficient to be detected by an intensified CCD camera.

Inset a of Fig. 12 shows a single-shot image obtained in ambient air. Since the grating has been formed in an isotropic medium no structure should be visible. The inhomogeneities observed in the image arise from the intensity profile of the Nd:YAG laser. Apart from this pattern, which is caused by poor alignment of the laser, local shot-to-shot intensity fluctuations in the signal beam have to be taken into account. From comparison of several images recorded subsequently in air, the size of these intensity fluctuations has been estimated to be roughly $\pm 10\%$.

The LIG image is generated in the overlap region of the circular-shaped excitation beam EB1 and the laser sheet formed by the probe beam and the excitation beam EB2. Therefore, the observation area is an oval. If the CCD camera is placed normal to the propagation direction of the circular excitation beam, the monitored area is compressed to a circular image. The compression factor is $\sin\theta$ for the axis lying in the plane formed by the wave vectors of the two excitation beams. The image distortion caused by this foreshortening has not been accounted for in this work. As a matter of fact, the use of large crossing angles would be advantageous for an improved spatial resolution and less distortion of the image. Ideally, to avoid any distortion of the obtained image, the crossing angle θ of the excitation beams should be equal to $90°$. This would lead, however, to a significant reduction of the grating spacing and to a correspondingly shorter lifetime of the LIG.

Due to the smaller electrostrictive constant γ_e the electrostrictive LIG signal obtained in helium is reduced by a factor of 66 compared to a signal generated in air. Therefore, the main contribution in a mixture of air and helium is originating from air. Inset b of Fig. 12 depicts a single-shot image of a helium flow in air. In the colored scale representation the areas of high helium concentration are displayed brightly, while the atmospheric air regions are dark. Since the laser intensity is not homogeneous across the beam profile, the image has been corrected by a reference image obtained in air. Of course, this correction cannot account for shot-to-shot laser intensity fluctuations since the two images result from two different laser shots. The intensity values of the corrected image are normalized between zero and unity, corresponding to an air partial pressure lower than 30 mbar and 1 bar, respectively. The local fluctuations of the electrostrictive signal intensity due to shot-to-shot fluctuations of the laser intensity yield an error of about 7% for the determination of the air partial pressure. Note that no care has been taken to establish a laminar helium flow. Hence, the observed structures may have been caused by the turbulent streaming of helium as well as by the movements of the surrounding air.

In addition, the technique has been applied to image sooty flames. For this purpose an acetylene/air diffusion flame has been used. The fuel–air mixture fraction in the flame is set just below the point of soot formation. Soot particles and soot precursors absorb widely across the electromagnetic spectrum. In particular, the extinction losses of the incident laser radiation in the flame due to absorption or scattering are measured to be about 20% over the intensity range from 15 MW/cm^2 to 90 MW/cm^2. It is thus possible to generate very efficiently thermal gratings in sooty flames with almost any pulsed laser system. These gratings can be used to map soot-particle concentrations, as is proposed in our work [20], or to measure the flame temperature [54].

The regions of high soot concentration in a laminar acetylene/air diffusion flame can easily be recognized by eye due to a bright yellow emission. The thermal LIG signal formed in these areas is strong enough to be readily observed by the naked eye when directed on to a piece of paper. For the grating generated in the sooty flame a diffraction efficiency of $\eta = (3.0 \pm 1.0) \times 10^{-4}$ is measured at a laser output intensity of 90 MW/cm^2. The inset of Fig. 13 shows a single-shot image of an axis-symmetric acetylene/air diffusion flame. This image has also been corrected by a reference image recorded in air. The regions with high particle concentration are displayed brightly. The observed distribution reflects the shape of the fuel/air reaction zone. Note that on the left-hand side of the image the signal intensity is higher than on the right-hand side since 20% of the probe beam has been absorbed. No attempt has been made for a quantitative interpretation of this image.

Soot particles in the flame absorb the incident laser radiation and are heated to temperatures far above ambient. There are two mechanisms involved by which the soot particles lose their internal energy absorbed from the laser. Below 3300 K heat conduction is the dominant loss process. Above 3300 K,
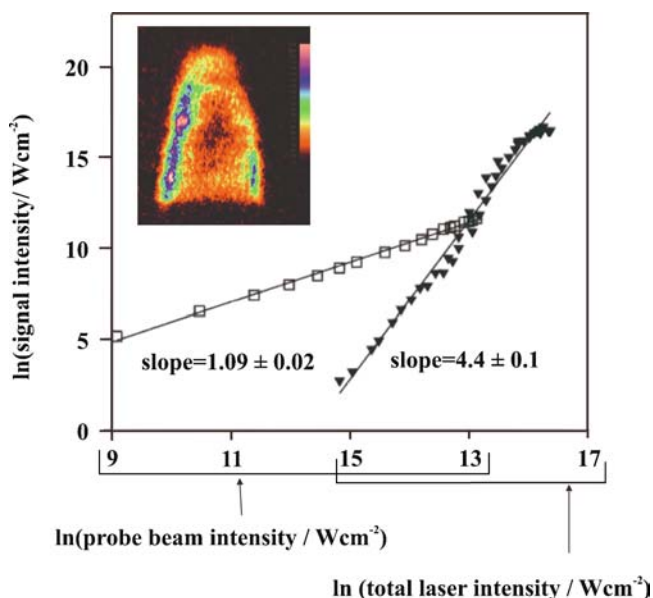
FIGURE 13 LIG signal intensity dependence vs. the laser intensity. The measurements are performed in an acetylene/air sooty flame. *Open squares*: signal intensity dependence vs. the probe beam intensity. *Solid triangles*: signal intensity dependence vs. the total laser intensity. *Inset*: single-shot image of an axis-symmetric acetylene/air diffusion flame. The flame is about 8-mm high and 6-mm wide. The colored scale reflecting the particle concentration is given in arbitrary units

soot vaporization prevails. The large heat of vaporization of carbon prevents the particles from reaching temperatures far above the vaporization point, rendering the heat loss by radiation unimportant. Therefore, at high temperatures the absorbed laser energy is balanced by vaporization that causes a mass reduction of the soot particles. Figure 13 shows a double-logarithmic plot of the intensity of the LIG signal generated in the sooty flame vs. the total laser intensity. The data has been fitted by a linear regression with a slope of 4.4 ± 0.1 (solid triangles). Furthermore, a linear dependence of the signal generated in a sooty flame upon the probe beam intensity has been measured (open squares in Fig. 13). The vaporization of the soot particles yields mainly C_3, C_2, and C. Since the wavelength of the excitation and probe beams at 532 nm is very close to a transition in C_2 ($d^3\Pi_g \leftarrow a^3\Pi_u$, $v' = 0$, $v'' = 0$), the observed signal includes contributions originating from solid soot particles as well as from C_2 that has been generated by vaporization. The high-order (≥ 3) signal dependence upon the excitation beams reflects the complex formation process of the signal [55].

3   Summary and conclusions

The main goal of the studies reviewed here and in the companion paper [1] was to investigate the potential of electrostrictive and thermal LIGs for diagnostics in the gas phase. Accordingly, an important part of this work is devoted to understand the formation mechanisms of such gratings generated in the gas phase; see Ref. [1].

In this article we focus on the applicability of the LIG technique for the diagnostics in the gas phase. The first diagnostic application presented is thermometry. The adiabatic

sound velocity is easily inferred from the frequency analysis of the oscillating part of the grating diffraction efficiency. For a known composition of the medium, the temperature is deducible from the measured sound velocity. Taking advantage of the non-resonant nature of electrostrictive gratings, we showed that the determination of temperatures in any gas by single-shot measurements is feasible. The experimental setup as well as the data analysis of the electrostrictive and thermal LIG techniques is relatively simple compared to other thermometry methods. Consequently, electrostrictive and thermal grating methods have the potential to become a valid alternative to classical laser-based thermometry techniques, especially in high-pressure environments where the damping of the acoustic waves is low. It is important to mention, however, that the measured sound velocity and therefore the temperature relies on the accurate determination of the intersection angle of the two excitation beams. To circumvent this problem a reference measurement is required for calibration. In turbulent environments, however, shot-to-shot variations of the crossing angle may occur due to beam-steering effects. Another drawback of the LIG technique is its poor spatial resolution, especially along the beams' propagation directions. In the experiments reviewed in this article the capability of electrostrictive and thermal LIGs to measure the temperature in air at atmospheric pressure up to 1400 K and in different flat flames in the pressure range between 1 and 25 bar has been tested. Good agreement between the LIG air temperatures and the thermocouple values has been found. Up to a pressure of 10 bar the flame temperatures obtained using the LIG technique agree well with CARS measurements and theoretical modeling. The discrepancy occurring at higher pressures is probably due to beam-steering effects and further experiments are necessary to clarify the issue. In fact, a systematic investigation of temperature measurements by laser-induced thermal gratings validated by simultaneous CARS measurements is mandatory in order to promote the laser-induced grating technique as a powerful alternative to other established methods for laser-based thermometry.

A further diagnostic application reviewed in this work is the use of LIGs for the determination of concentrations. By measuring the sound velocity, laser-induced electrostrictive gratings have been applied to monitor the variation in concentration of binary gas mixtures of known temperature as small as 0.5–2%. The advantage of a relatively undemanding experimental setup is somewhat lessened by the loss in species selectivity. Additionally, the sensitivity is decreased for similar sound velocities of the mixture components and is, therefore, limited to some extent.

For the detection of trace-gas species it was shown to be more advantageous to apply thermal LIGs, since the method is found to be highly sensitive in environments where quenching is predominant. As a demonstration we have applied thermal LIGs to detect the isotopic molecule $^{16}O^{18}O$ in its natural abundance. For quantitative measurements the dependence of the thermal grating signal on pressure, temperature, and gas composition has to be known owing to the strong dependence of the method on quenching processes.

Another important application of thermal LIGs reviewed in this article is the study of multistage collisional relaxation processes in gases. For this purpose thermal LIGs have

been excited by direct absorption of O_2 and by addressing Raman transitions in CO_2. Selective excitation of rovibronic or vibrational molecular transitions affects the temporal evolution of the LIG diffraction efficiency since the relaxation pathways, the magnitude, and the sign of the exchanged energy depend upon the pumped molecular level. The analysis of the temporal evolution of LIGs' diffraction efficiency allowed us to distinguish different contributions (population, thermal, electrostrictive) to the signal and provided information on the molecule-dependent pathways of absorbed laser energy relaxation as well as values of effective rates and exchanged energies. These results agree reasonably well with known data from the literature which have been obtained by other methods. We conclude that thermal gratings have the potential to provide insight into inter- and intramolecular energy transfer and in this aspect they are comparable with more traditional methods like photoacoustic spectroscopy. Due to its dependence on quenching, thermal grating spectroscopy is supplementary to laser-induced fluorescence.

One of the most appealing features of this technique is to allow for the simultaneous, instantaneous, and non-intrusive measurements of temperature and flow velocities. Such measurements might be useful for the investigation of wind tunnels or the premixing zone of large-scale burners. In this work, the technique has been used to measure simultaneously temperatures in the range of 295–600 K and flow velocities in the range of 10–100 m/s in a submerged air jet. From the experiments described here, we conclude that the electrostrictive laser-induced grating technique is particularly suited for studying the high-speed flow in a relatively high-density, low-temperature medium exhibiting a limited degree of turbulence. The lower limit of the measurable flow velocities is due to the short decay time of the LIGs at atmospheric pressure. In a future work, we plan to overcome this problem by seeding the flow with a long-lived stationary density wave, resulting from a slow heat-release process generating a thermal LIG.

Finally, the imaging potential of the laser-induced grating technique has been investigated. A planar backward geometry has been used to produce images. A circular pump beam intersects the second pump and the probe beam that are both shaped into a thin light sheet. Single-shot images of a helium flow submerged in ambient air by electrostrictive gratings have been recorded, proving the applicability of this technique for remote two-dimensional diagnostics of a gas-mixing processes without seeding. Furthermore, thermal gratings have been applied to map the particle concentration in a sooty flame. The oxidant–fuel reaction zone is readily visualized by single-shot measurements. However, in order to perform quantitative measurements, the mechanism of the interaction between the soot present in the flame and the strong laser radiation needs to be investigated in more detail.

REFERENCES

1 A. Stampanoni-Panariello, D.N. Kozlov, P.P. Radi, B. Hemmerling, Appl. Phys. B (2005), DOI 10.1007/s00340-005-1852-z
2 A.C. Eckbreth, *Laser Diagnostics for Combustion Temperature and Species* (Abacus, Cambridge, 1988)
3 B. Hemmerling, R. Bombach, W. Hubschmid, Chem. Phys. Lett. **256**, 71 (1996)
4 D.N. Kozlov, R. Bombach, B. Hemmerling, W. Hubschmid, Opt. Commun. **166**, 245 (1999)
5 R. Fantoni, M. Giorgi, L. De Dominicis, D.N. Kozlov, Chem. Phys. Lett. **332**, 375 (2000)
6 W. Hubschmid, B. Hemmerling, Chem. Phys. **259**, 109 (2000)
7 B. Hemmerling, D.N. Kozlov, Chem. Phys. **291**, 213 (2003)
8 S. Schlamp, H.G. Hornung, Th. Sobota, E.B. Cummings, Appl. Opt. **39**, 5477 (2000)
9 Y. Kimura, D. Kanda, M. Terazima, M. Hirota, Ber. Bunsenges. Phys. Chem. **99**, 1850 (1995)
10 H. Latzel, T. Dreier, M. Giorgi, R. Fantoni, Ber. Bunsenges. Phys. Chem. **101**, 1065 (1997)
11 D.A. Greenhalgh, in *Advances in Non-Linear Spectroscopy*, vol. 15, ed. by R.J.H. Clark, R.E. Hester (Wiley, Chirchester, 1998), p. 193
12 S. Williams, L.A. Rahn, P.H. Paul, J.W. Forsman, R.N. Zare, Opt. Lett. **19**, 1681 (1994)
13 P.F. Barker, J.H. Grinstead, R.B. Miles, Opt. Commun. **168**, 177 (1999)
14 S. Schlamp, E.B. Cummings, T.H. Sobota, Opt. Lett. **25**, 224 (2000)
15 S. Schlamp, T.H. Sobota, Exp. Fluids **32**, 683 (2002)
16 M.S. Brown, W.L. Roberts, J. Propuls. Power **15**, 119 (1999)
17 K.A. Nelson, D.R. Lutz, M.D. Fayer, L. Madison, Phys. Rev. B **24**, 3261 (1981)
18 K.A. Nelson, R.J.D. Miller, D.R. Lutz, M.D. Fayer, J. Appl. Phys. **53**, 1144 (1982)
19 Y. Yan, K.A. Nelson, J. Chem. Phys. **87**, 6240 (1987)
20 B. Hemmerling, A.C. Stampanoni-Panariello, Appl. Phys. B **57**, 281 (1993)
21 E.B. Cummings, Opt. Lett. **19**, 1361 (1994)
22 A.C. Stampanoni-Panariello, B. Hemmerling, W. Hubschmid, Phys. Rev. A **51**, 655 (1995)
23 A.C. Stampanoni-Panariello, B. Hemmerling, W. Hubschmid, Appl. Phys. B **67**, 125 (1998)
24 B. Hemmerling, D.N. Kozlov, Appl. Opt. **38**(6), 1001 (1999)
25 B. Hemmerling, W. Hubschmid, A. Stampanoni-Panariello, in *27th (International) Symposium on Combustion*, 2–7 August 1998 Boulder, Colorado USA, vol. 1 (The Combustion Institute, Pittsburgh, Pensylvania, 1998), p. 69
26 B. Hemmerling, W. Hubschmid, D.N. Kozlov, A. Stampanoni-Panariello, in *Laser Spectroscopy and Optical Diagnostics: Novel Trends and Applications in Laser Chemistry, Biophysics, and Biomedicine:* ICONO'98, 29 June–3 July 1998, Moscow, Russia, vol. 10, Proc. of SPIE 3732 (Bellingham, Washington, SPIE, 1999), p. 3732
27 B. Hemmerling, D.N. Kozlov, A. Stampanoni-Panariello, Opt. Lett. **25**, 1340 (2000)
28 D.N. Kozlov, B. Hemmerling, A.C. Stampanoni-Panariello, Appl. Phys. B **71**, 585 (2000)
29 D.N. Kozlov, B. Hemmerling, R. Bombach, W. Hubschmid, Opt. Lett. **22**, 46 (1997)
30 B. Hemmerling, M. Neracher, D. Kozlov, W. Kwan, R. Stark, D. Klimenko, W. Clauss, M. Oschwald, J. Raman Spectrosc. **33**, 912 (2002)
31 M. Péalat, M. Lefebvre, Appl. Phys. B **53**, 23 (1991)
32 R.C. Hart, R.J. Balla, G.C. Herring, Appl. Opt. **38**, 577 (1999)
33 A. Arnold, R. Bombach, B. Käppeli, A. Schlegel, Appl. Phys. B **64**, 579 (1997)
34 A. Lawitzki, I. Plath, W. Stricker, J. Bittner, U. Meier, K. Kohse-Höinghaus, Appl. Phys. B **50**, 513 (1990)
35 HITRAN database http://cfa-www.harvard.edu/HITRAN/
36 E. Cummings, Opt. Lett. **19**, 1361 (1994)
37 A.C. Boccara, D. Fournier, J. Badoz, Appl. Phys. Lett. **37**, 130 (1979)
38 J.R. Barker, B.M. Toselli, in *Photothermal Investigations of Solids and Fluids*, ed. by J.A. Sell (Academic Press, Boston, MA, 1989), p. 155
39 J.J. Barrett, Appl. Spectrosc. Rev. **21**(4), 419 (1985)
40 J.R. Andrews, R.M. Hochstrasser, Chem. Phys. Lett. **76**, 207 (1980)
41 R. Wayne, *Singlet O_2*, vol. 1, ed. by A.A. Frimer (CRC, Boca Raton, FL, 1985)
42 H.D. Babcock, L. Herzberg, Astrophys. J. **8**, 167 (1948)

43 J.H. Miller, R.W. Boese, L.P. Giver, J. Quantum Spectrosc. Radiat. Transfer **9**, 1507 (1969)

44 A.M. Brodnikovskii, S.M. Gladkov, M.G. Karimov, N.I. Koroteev, Soviet Physics JETP **57**, 971 (1983)

45 F. Lepoutre, G. Louis, H. Manceau, Chem. Phys. Lett. **48**, 509 (1977)

46 C. Allen, T.J. Price, C.J.S. Simpson, Chem. Phys. Lett. **45**, 183 (1977)

47 B. Scherrer, A. Godard, I. Ribet, P. Bouchardy, T. Pot, M. Lefebvre, Appl. Phys. B **71**, 859 (2000)

48 S. Schlamp, E.B. Cummings, H.G. Hornung, Appl. Opt. **38**, 5724 (1999)

49 D.J.W. Walker, R.B. Williams, P. Ewart, Opt. Lett. **19**, 1681 (1994)

50 I. Ribet, B. Scherrer, P. Bouchardy, T. Pot, J.P. Taran, M. Lefebvre, J. Raman Spectrosc. **31**, 689 (2000)

51 Encyclopédie des Gaz. L'Air Liquide, Elsevier Science Publishers, B.V., Amsterdam, (1976)

52 D.J. Rakestraw, R.L. Farrow, T. Dreier, Opt. Lett. **15**, 709 (1990)

53 *Laser Operation and Maintenance Manual NY80, 81, 82* (Continuum, Santa Clara, CA, 1990)

54 M.S. Brown, W.L. Roberts, J. Propuls. Power **15**, 119 (1999)

55 B. Hemmerling, A. Stampanoni-Panariello, Chemosphere **42**, 647 (2001)